The Crop Journal 12 (2024) 614–629

Contents lists available at ScienceDirect

The Crop Journal

journal homepage: www.keaipublishing.com/en/journals/the-crop-journal/

Mapping upland crop–rice cropping systems for targeted sustainable intensification in South China

Bingwen Qiu [a,*], Linhai Yu [a], Peng Yang [b], Wenbin Wu [b], Jianfeng Chen [a], Xiaolin Zhu [c], Mingjie Duan [c]

[a] Key Laboratory of Spatial Data Mining &Information Sharing of Ministry of Education, Academy of Digital China (Fujian), Fuzhou University, Fuzhou 350116, Fujian, China
[b] Key Laboratory of Agricultural Remote Sensing, Ministry of Agriculture and Rural Affairs, Beijing 100081, China
[c] Department of Land Surveying and Geo-Informatics, The Hong Kong Polytechnic University, Kowloon 999077, Hong Kong, China

ARTICLE INFO

Article history:
Received 10 October 2023
Revised 28 December 2023
Accepted 29 December 2023
Available online 23 March 2024

Keywords:
Cropping-pattern mapping
Paddy rice
Sentinel-1/2
China
Sustainable intensification

ABSTRACT

Upland crop-rice cropping systems (UCR) facilitate sustainable agricultural intensification. Accurate UCR cultivation mapping is needed to ensure food security, sustainable water management, and rural revitalization. However, datasets describing cropping systems are limited in spatial coverage and crop types. Mapping UCR is more challenging than crop identification and most existing approaches rely heavily on accurate phenology calendars and representative training samples, which limits its applications over large regions. We describe a novel algorithm (RRSS) for automatic mapping of upland crop–rice cropping systems using Sentinel-1 Synthetic Aperture Radar (SAR) and Sentinel-2 Multispectral Instrument (MSI) data. One indicator, the VV backscatter range, was proposed to discriminate UCR and another two indicators were designed by coupling greenness and pigment indices to further discriminate tobacco or oilseed UCR. The RRSS algorithm was applied to South China characterized by complex smallholder rice cropping systems and diverse topographic conditions. This study developed 10-m UCR maps of a major rice bowl in South China, the Xiang-Gan-Min (XGM) region. The performance of the RRSS algorithm was validated based on 5197 ground-truth reference sites, with an overall accuracy of 91.92%. There were 7348 km^2 areas of UCR, roughly one-half of them located in plains. The UCR was represented mainly by oilseed-UCR and tobacco-UCR, which contributed respectively 69% and 15% of UCR area. UCR patterns accounted for only one-tenth of rice production, which can be tripled by intensification from single rice cropping. Application to complex and fragmented subtropical regions suggested the spatiotemporal robustness of the RRSS algorithm, which could be further applied to generate 10-m UCR datasets for application at national or global scales.

1. Introduction

Agricultural systems are currently facing a series of challenges associated with achieving Sustainable Development Goals (SDGs) and alleviating the environmental consequences of cropping practices [1]. Paddy rice, which feeds more than half of the global population [2], is responsible for one fourth to one third of global freshwater consumption and one tenth of methane emissions [3]. Sustainable agriculture through improved cropping practices can benefit food production and the environment [4,5]. Location and crop-specific Cropping Patterns (CP), the sequences of annual crops, is one of the key cropping practices for sustainable intensification [6]. Agricultural intensification can be promoted by development of multiple cropping patterns without cropland expansion [7]. Context-specific strategies for major cropping systems are needed to facilitate resilient agricultural systems [8,9]. Spatiotemporal data on cropping patterns is vital for sustainable land management [10,11].

Cropping patterns can be categorized into monocropping and multiple cropping according to the cropping frequency per year. Multiple cropping systems with various crops (such as winter wheat–rice) have been widely employed in agricultural management for its benefits of improving soil quality and reducing disease incidence [12]. China is the world's largest rice producer and rice is commonly cultivated in small paddy fields with diverse crop cycles [13]. Oilseed in China accounts for about 20% of world production [14]. The Upland Crop-Rice (UCR) cropping system of oilseeds and rice, a common cropping practice in the Yangtze River basin of China, improves rice yield and soil quality [15]. Other UCR

* Corresponding author.
E-mail address: qiubingwen@fzu.edu.cn (B. Qiu).

https://doi.org/10.1016/j.cj.2023.12.010

practices include winter wheat–rice, tobacco–rice and vegetable–rice. China is the largest wheat and tobacco producer in the world. Winter wheat is commonly double-cropped followed by maize or paddy rice in eastern China [16,17]. Tobacco–rice cropping system is used in mountainous and hilly regions of southern China and supports rural vitalization. But few accurate, finer-resolution UCR maps with rotated crop types are available on regional scales (> 1000 km^2), especially in smallholder agricultural systems [18]. Detailed information on cropping patterns is rarely reported in agricultural statistics [6].

Remote sensing has permitted monitoring of changes in agricultural practice over large spatial domains [19]. Agricultural remote sensing studies can be grouped into three categories. The first group estimates the cropping intensity of all crops cultivated per year [20,21] and the second group concentrates on the cropping intensity of one specific crop [22]. The third group provides detailed information on cropping intensity as well as the sequence of cultivated crop types [16,23]. Most existing large-scale studies of cropping patterns fall within the first two groups, and were conducted primarily based on optical images such as the MODIS and Landsat time series images [24,25].

Mapping cropping sequences is more challenging than crop identification [6]. Information on crop sequences is generally derived based on maps independently produced across multiple seasons or years [18,26]. Classification errors in the maps reduce the consistency of detection of cropping systems [5]. Descriptions of cropping systems with information on crop sequences are rarely available in developing countries with complex multiple cropping systems [23]. Most studies have investigated single-cropping regions, and only a few studies have investigated complex multiple cropping systems [23,27]. Datasets on cropping systems are still very limited in spatial coverage and crop types [1]. Automatic and robust mapping approaches are required for direct identification of complex multiple cropping patterns such as UCR over large spatial domains [1]. There is a lack of knowledge of the extent and locations of cropping patterns in complex agricultural systems [28]. Until now, little work has been performed on mapping UCR practices in comparison with other multiple cropping patterns such as upland–upland (winter wheat–maize) or double rice cropping systems.

The objectives of this study were to develop a robust UCR mapping algorithm by combining optical and SAR time series datasets, with the purpose of answering two questions: 1) What are the major challenges for automatic large-scale crop mapping over tropical/subtropical regions? 2) Could simple and robust crop mapping indices be developed to automatically extract information about crop types and cropping sequences, and how?

2. Study area and data sources

2.1. Study area

The study area (XGM region, 23°31′N–30°08′N, 108°47′E–120°43′E), located in South China, includes the Hunan (Xiang), Jiangxi (Gan) and Fujian (Min) provinces (Fig. 1A, B). The XGM region has a total land area of 502,700 km^2, three fourths of it located in mountains and hills. Roughly one-half of the cropland (47%) is distributed among mountains and hills in the XGM region. The XGM region is characterized by a subtropical monsoon humid climate with abundant heat and water resources, supporting multiple cropping such as of double rice the UCR. The region experiences an average annual temperature ranging from 17 to 20 °C, enjoys a frost-free period of over 250 d, and receives more than 1300 mm of precipitation annually. There are plains in the northeast of Hunan province and the central of Jiangxi province. The two largest lakes in China, Dongting and Poyang Lakes, are located in the northern portions of Hunan and Jiangxi provinces (Fig. 1B). Fujian province is characterized as a mountainous and hilly region, which has ranked the first in forest cover rate in China for 40 years [21]. Mountainous terrain is the main reason for low mapping accuracy in existing rice data products [30].

The XGM region accounted for 26.7% of the total paddy rice sown area in China according to the Agricultural Census Data in 2021 (http://tjj.hunan.gov.cn/, http://tjj.jiangxi.gov.cn/, http://tjj.fujian.gov.cn/). The Hunan and Jiangxi provinces rank first and third in rice production in China (Heilongjiang province in Northeast China ranked second, but cannot be cultivated by multiple cropping owing to temperature limits). Paddy rice accounts for 85% of grain production in the study area (Fig. 1A). There are three kinds of rice cropping patterns defined by cropping intensity and crop sequences are single rice cropping, double rice, and UCR. The multiple cropping systems of UCR commonly feature a sequence of winter crops such as oilseed, tobacco and vegetables, followed by paddy rice cultivated in summer in the XGM region (Fig. 1F). The XGM region accounted for respectively 26.6% and 14.7% of oilseed and tobacco sown areas in China (Fig. S1). Specifically, Hunan province ranks at the top in oilseed production in China. Compared to rice and oilseed, the tobacco industry makes much higher profits. The Gross domestic product (GDP) of tobacco is commonly transplanted during late February, enters the early vegetative growth stages (reunion period) after 10–15 d, then experiences rapid vegetative growth stage (around one month) in April, and finally the maturing stage during summer (May and June) (Fig. S1). The growing period of tobacco spans around 130 d from transplanting to harvesting. Although tobacco is commonly harvested for its leaves, the maturing stage is fairly long, covering almost half of the growing season. The oilseed is commonly planted in October and then experiences a long of (around two months) vegetative stage during the winter. The budding period of oilseed starts in the early or middle of January, the flowering stage continues for more than one month, and harvesting season ranges between late April and early June (Fig. S1).

2.2. Datasets

2.2.1. Sentinel-1 SAR images

Sentinel-1 SAR images were applied in this study. All available level-1 Ground Range Detected (GRD) products in the XGM region were used, including respectively 971 and 947 Sentinel-1 GRD images in 2018 and 2021. Sentinel-1 GRD images have a spatial resolution of 10 m and a revisit frequency of 12 d. The Sentinel-1 GRD product is in Interferometric Wide Swath mode with dual-band cross-polarization (VV) and vertical transmit/horizontal receive (VH). VV is sensitive to both volume and surface scattering [31]. This study characterized the upland crop-rice cropping systems based on the changes in crop and ground parameters. Therefore, the VV backscattering coefficients time series was applied and smoothed with a Whittaker smoother [32] (WS) (lambda = 1, order = 2). Data preprocessing and the mapping algorithm were implemented in the Google Earth Engine (GEE) platform in this study.

2.2.2. Sentinel-2 MSI images

The Sentinel-2 MSI time series images offer great opportunities for agricultural mapping due to their improvements in spatial, temporal and spectral resolutions (3 unique red-edge bands) [33]. We collected all available Level-1C Sentinel-2A/B images, constituting respectively 9479 and 10,371 Sentinel-2 MSI images in 2018 and 2021. For each pixel, invalid observations with cloud contamination were discarded. Spectral indices were calculated

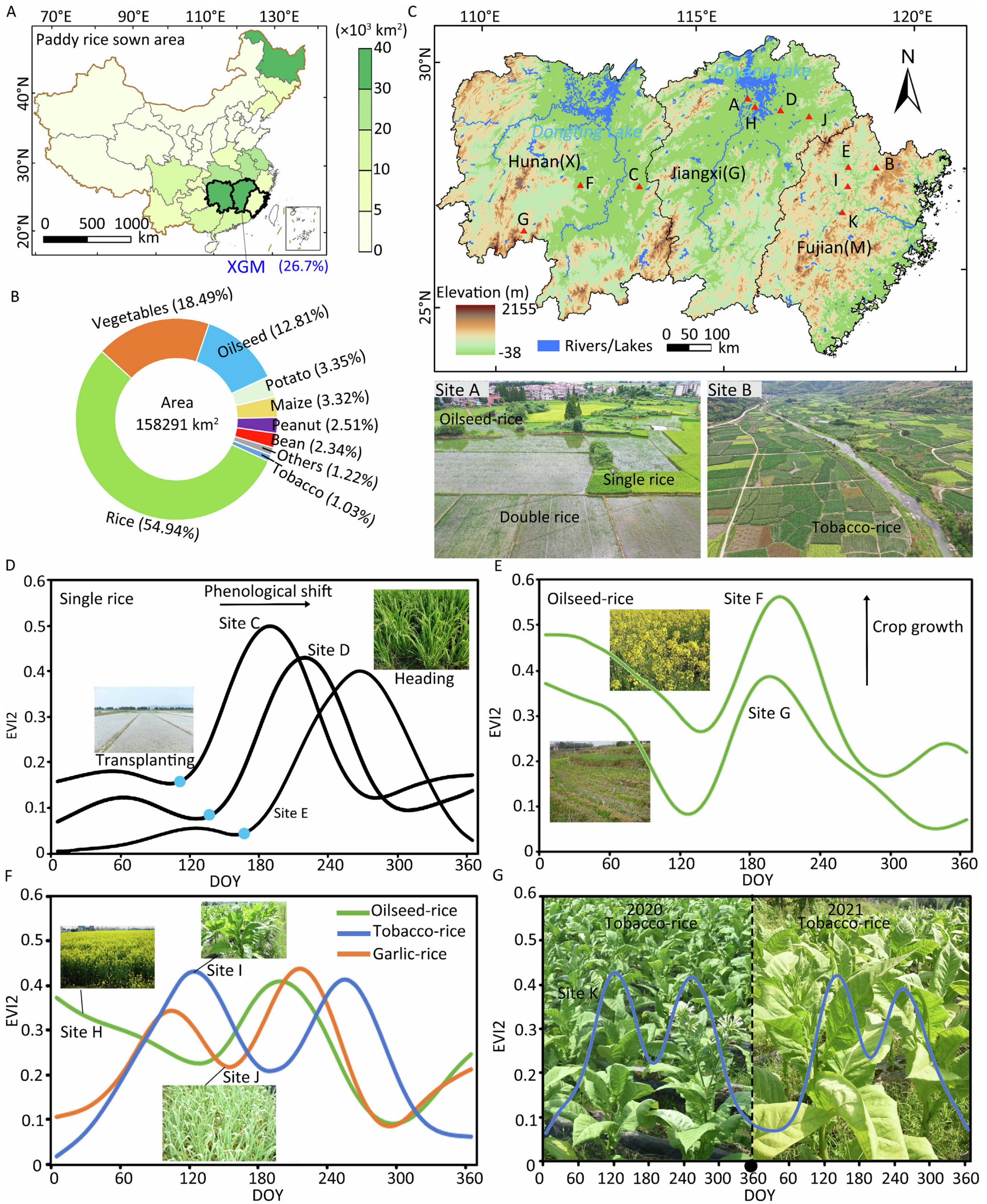

Fig. 1. Maps of study area and intra-class variability of cropping patterns. (A) rice sown area in China and (B) the proportions of crops in the XGM region in 2021; (C) elevation, some reference sites, and field photos; (D) phenological shifts; (E) growth status; (F) cropping patterns; (G) inter-annual variations. The authors declared that boundary of China map is totally based on the Audit Number: GS (2020) 4234 without re-editing.

and a smoothed 10-day composite time series of spectral indices was obtained using a WS with lambda 10 and order 2.

Two spectral indices were computed: a two-band Enhanced Vegetation Index (EVI2) [34] and an Anthocyanin Reflectance Index (ARI) [35]. Higher values in ARI represent higher concentrations of anthocyanin. The vegetation and pigment indices were calculated using equations 1–3.

$$\mathrm{EVI2} = 2.5 \times \left(\rho_{\mathrm{NIR}} - \rho_{\mathrm{Red}}\right) \Big/ \left(\rho_{\mathrm{NIR}} + 2.4 \times \rho_{\mathrm{Red}} + 1\right) \tag{1}$$

$$\mathrm{ARI} = \frac{1}{\rho_{\mathrm{Green}}} - \frac{1}{\rho_{\mathrm{VRE1}}} \tag{2}$$

$$\mathrm{CIre} = \frac{\rho_{\mathrm{NIR}}}{\rho_{\mathrm{VRE1}}} - 1 \tag{3}$$

Here, ρ_{NIR}, ρ_{Red}, ρ_{Green} and ρ_{VRE1} represent top-of-atmosphere reflectance (TOA) values from the Near-infrared, Red, Green and Vegetation Red Edge 1 (VRE1) in Sentinel-2 images.

2.2.3. Ground-truth reference data, agricultural census data, and other datasets

Ground truth reference data were obtained primarily through field surveys. Field surveys have been conducted across these three provinces since 2018. At each survey site, the position was recorded along with crop types, cropping patterns, and the corresponding phenological stages and field photos. Among the 7206 ground-truth sites (Fig. S3), 2178 were implemented by UCR: 927 of oilseed–rice, 701 of tobacco–rice, and other UCR combinations including vegetable–rice and maize–rice). Other cropping patterns included single cropping of paddy rice, peanut, soybean, and sweet potato, double cropping of double rice and oilseed–maize/cotton, and other patterns such as single maize and vegetables. Approximately 30% (2009) of the reference sites were selected for determining thresholds in the mapping decision rule and 70% (5197) of the reference sites were used for accuracy assessment.

The agricultural census data, detailing the total sown area of major crops, were obtained from statistical yearbooks available on the official websites of various provincial statistics bureaus. For example, the statistical yearbook in Hunan province in 2022 (http://tjj.hunan.gov.cn/) reported the planting areas of paddy rice, oilseed or tobacco by prefecture in 2021. However, because the statistical yearbook provided no information on specific cropping patterns, these data (http://tjj.jiangxi.gov.cn/, http://tjj.fujian.gov.cn/) were merely used to estimate the extent of UCR in rice cultivation in the study area. Other datasets included cropland distribution data and crop calendar data. The cropland distribution dataset was derived from the 2020 GlobelLand30 dataset [36], which is the first 30 m-resolution global land cover dataset with good accuracy. Crop calendar data were obtained from the National Meteorological Bureau of China (http://data.cma.cn) and also collected during fieldwork.

3. Methodology

3.1. Problems of crop mapping over fragmented subtropical regions

Research efforts have been applied to identifying a series of crops such as paddy rice and winter wheat [37,38]. The data-driven mapping algorithm has been increasingly employed for crop mapping, especially deep learning algorithms, which can automatically learn useful features for target classification [28,39]. However, these trained models driven by massive sample datasets are challenged by the capabilities of generalization across regions or years owing to differences in cropping systems, crop phenology, and other factors [40,41]. The phenological dates of crops are susceptible to changes in climatic conditions and planting patterns over large areas [42,43]. Crop mapping is challenged by intra-class variation in spectral and temporal features across regions and years [44]. Large-scale applications of supervised classification approaches are constrained by their limited transferring capabilities due to regional or temporal discrepancies [40].

There are at least two major challenges in crop mapping over fragmented subtropical regions with mixed single and double cropping systems. First, there is a lack of reliable and updated Cropping Intensity (CI) datasets with finer resolutions at large scales. These are commonly prerequisites of crop mapping frameworks in complex agricultural regions with multiple cropping. The number of crop growing cycles is determined and then key phenological stages such as the flowering stage are estimated to identify the proper time phase for discriminating among crops [45]. CI mapping is implemented primarily based on the temporal curves of vegetation indices such as the NDVI or EVI [24,46,47]. However, it is difficult to establish a relationship between VI curves and cropping cycles over large regions with complex and diverse agricultural systems [20]. Existing cropping intensity datasets are available only at coarse resolutions or in limited years, and show large uncertainties in humid subtropical regions [46,48].

Second, there are large and inevitable intraclass variation and inter-class similarities in spectral and temporal features across regions and years [28]. There are at least two kinds of intraclass variation, one (group I) associated with changes in crop phenology, and the other (group II) with crop growth. It is commonly observed [40,42] that the phenology of the same crop varies across regions and years, following changes in climatic conditions and cultivation history. The crop calendar of the same crop could be flexible and changeable even within small areas, especially among tropical or subtropical regions with abundant water and heat resources. For example, a single crop of paddy rice can be transplanted from April to August in southern China (Fig, 1D). Differences in crop growth can be introduced by changes in cropland quality and cropping activities such as irrigation and fertilization (Fig. 1E). There are large discrepancies in VI values of the same crop and similarities across vegetation types [20,43]. These two groups of intraclass variation can persist across years (Fig. 1G) and are further exacerbated by the inconsistency of data availability. Optical time-series images are influenced by cloud contamination, especially in humid and cloudy regions [43]. These spatiotemporal heterogeneities in the same crop can severely degrade the performances of existing crop mapping algorithms [18]. In summary, agricultural remote sensing applications are more challenging in tropical and subtropical regions than in other climatic regions.

3.2. Overview of the framework: Moving from crop mapping to cropping pattern identification

The rice cropping pattern, the UCR, and two major UCR types (oilseed–UCR, tobacco–UCR), were mapped based on Sentinel-1 SAR and Sentinel-2 MSI time series (Fig. 2). First, the double-cropping pattern of UCR was characterized by the large change magnitude of VV signals. We developed a new UCR indicator by accounting for the inter-seasonal feature of UCR introduced by upland crop cultivation (high VV at heading stage) rotated with paddy rice (low VV in the transplanting stage) in the Sentinel-1 VV time series. Second, multiple UCR patterns were further depicted using vegetation, chlorophyll, and anthocyanin indices based on the Sentinel-2 MSI time series. Finally, We present an innovative algorithm (RRSS) designed for the automatic mapping of upland crop–rice cropping systems by harnessing the capabilities of Sentinel-1 Synthetic Aperture Radar (SAR) and Sentinel-2

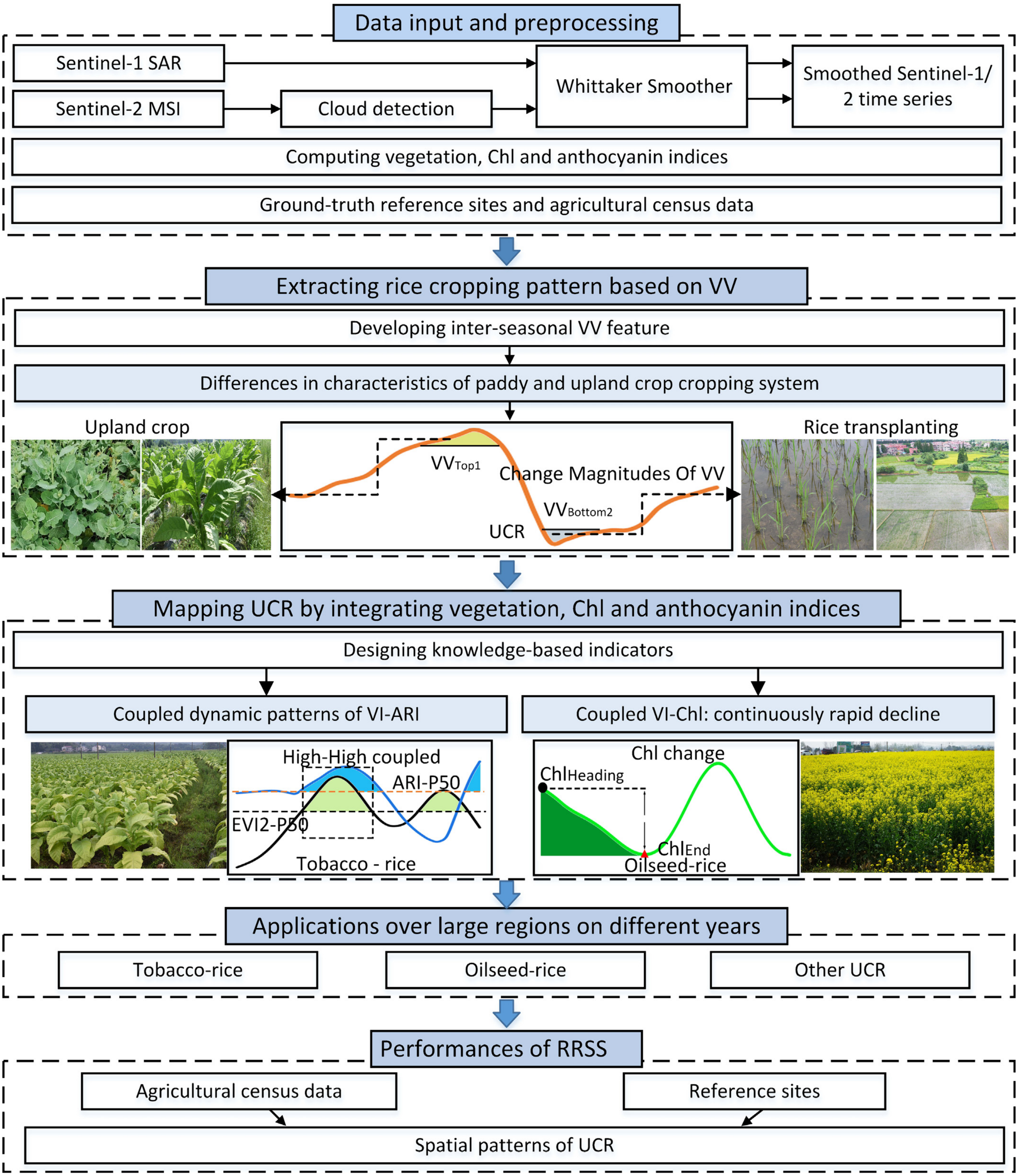

Fig. 2. The flow of the proposed RRSS algorithm.

Multispectral Instrument (MSI) data. Maps of UCR patterns could be derived based on the RRSS algorithm and validated using the reference data. These mapping procedures were implemented on the GEE platform.

3.3. Characterizing cropping patterns based on Sentinel-1 VV time series

3.3.1. Temporal profiles of VV backscatter from cropping patterns

The temporal profiles of Sentinel-1A VV backscatter from various land covers are shown (Fig. 3) based on selected sites. Non-vegetated land covers show either very high or very backscatter coefficients compared to vegetation, as observed in previous studies [49]. Among these vegetated areas, crops can be distinguished from other vegetation covers (such as forest land) by the greater variations of backscatter coefficients caused by cropping activities [50]. In particular, some studies [51,52] found that paddy rice can be discriminated from other crops by the higher dynamic ranges of coefficients in paddy fields.

The paddy rice fields are characterized by a dropping-rising V-shaped feature in Sentinel-1A VH/VV backscatter time trajectory rising from the flooding signals, which has been applied for rice mapping in recent studies [52,53]. In contrast, most upland crops such as maize and oilseed display an upside V (Λ) shape feature of VV backscatter during the growing season. The VV backscatters of maize experienced a dynamic increase corresponding to the development of leaves and stem elongation, followed by a decrease during senescence (Fig. 3). However, there is one exception: the winter wheat also illustrates a falling–rising V-shaped feature of VV backscatter during the growing season. For winter wheat, the VV backscatters increased during tillering (from November to the following February), decreased during stem elongation, and then increased during the reproductive stages from inflorescence to ripening (Fig. 3).

3.3.2. Designing a UCR indicator based on inter-seasonal VV variations

The UCR was characterized by a broad and deep V-shaped feature of VV backscatter across two growing seasons (Fig. 3). The V feature of VV backscatter from UCR was accounted for by the inverted-V shape feature of the upland crop in the first season followed by the V shape feature of paddy rice in the second season. The bottom of the broad V shape feature of the VV backscatter from the UCR is located in the rice transplanting season rising by flooding. The top and bottom of the VV backscatter from the UCR were strengthened by upland crop and paddy rice, respectively, in the UCR cropping systems. Therefore, the change magnitude of VV backscatter from the UCR was higher than that from other cropping patterns of upland crops (single upland crop such as single maize, double upland crops such as winter wheat-maize) or rice cropping sites (single rice or double rice) (Fig. 3).

A Cropping Pattern index was proposed for mapping UCR (CPU) based on the intra-seasonal variations in VV backscatter (Fig. 3). The indicator of CPU was defined as:

$$\mathrm{CPU} = \mathrm{VV}^{\mathrm{Top1}} - \mathrm{VV}^{\mathrm{Bottom2}} \tag{3}$$

Here $\mathrm{VV}^{\mathrm{Top1}}$ represents the mean values of VV subsets of the top 30% in the first growing season; $\mathrm{VV}^{\mathrm{Bottom2}}$ denotes the mean values of VV subsets of the bottom 30% in the second growing season. The top 30% values of VV temporal profiles in the first growing season corresponded to phenological stages with fully covered crop canopies the maturing stage of tobacco), which consistently showed higher values in VV signals (Fig. S1). The bottom 30% of the VV temporal profile values were associated with the phenological stages from transplanting to tillering. This period consistently exhibited lower VV values, attributed to the presence of water bodies mixed with rice plants. Analyzing the combinations of these two subsets from adjacent growing seasons effectively revealed the cultivation practices of UCR.

3.4. Developing CP indicators for mapping various kinds of UCR

3.4.1. Temporal profiles of vegetation and pigments indices from different cropping patterns

Crops demonstrate dynamic patterns from the vegetation indices' temporal profiles during the growing season. EVI2 commonly increases after emergence, reaches peaks during the heading stage and drops rapidly during the harvesting stages (Fig. 3). The temporal curves of vegetation indices such as the NDVI and EVI2 have been widely applied to discriminate among crops [37,38]. However, there are inter-class similarities among crops (Fig. 3).

The content of chlorophyll roughly followed synchronous dynamic patterns of EVI2, with slightly varying temporal gaps depending on the crop type. The chlorophyll content, vital for photosynthesis, declines when the plants mature [54]. Differing from chlorophyll, the content of anthocyanin and carotenoids is increased when plants grow from flowering to seeding and harvesting stages [55]. Anthocyanin and carotenoids are abundant in juvenile plants for protecting plants from being overexposed to environmental stress [55]. Thus, anthocyanin exhibited the opposite temporal patterns to EVI2: the peaks of ARI were observed during the emergence and harvesting seasons for several crops such as paddy rice, maize, and soybean (Fig. S2).

Tobacco was distinguished by coherent dynamic patterns of VI-ARI, which showed higher ARI values during the heading stages (Fig. 3). Tobacco showed a much lower chlorophyll concentration during the heading stage than other crops. These unique features of tobacco are associated with the crop growth characteristics and its special cropping practices such as flag-leaf removal. The life cycle of tobacco commonly includes phenological stages starting from germination, formation of side shoots, stem elongation, development of harvestable plant parts (ripening of leaves), inflorescence emergence, flowering, development of fruit, ripening of seed to termination of the crop (harvesting) under no intervention. However, differently from most crops, the leaves of tobacco are harvested instead of the seeds, and are used for the production of cigarettes. Farmers cut off the flag leaf and the flowers to obtain tobacco leaves of good quality (large and yellow). The content of chlorophyll in tobacco declines and the leaves gradually turn yellow after the flag leaves are removed. Thus, the canopies of tobacco are dominated by these yellow and big leaves.

The unique characteristic of oilseed is the long-lasting bright yellow flowers, which can be detected in remote sensing images. Recent studies have achieved great progress in oilseed mapping by proposing a canola/oilseed index using images of the flowering stage [56]. The foundation of the oilseed flowering-based mapping algorithms is accurate estimation of the flowering phenology and the availability of high-quality images during the flowering stage [57]. It is challenging to continuously detect oilseed flowering phenology due to the frequently cloudy and rainy weather in South China. Besides the unique yellow flowers, oilseed also illustrated distinctive characteristics compared to other crops. The Chl of oilseed continuously declined after opening or from budding stages, which was observed from the beginning of the year to the oilseed harvesting season. In contrast, spring or summer crops were predominately by Chl increase during that period (Fig. S2).

3.4.2. Designing CP indicators by coupling temporal patterns of vegetation and pigment indices

We developed two indicators for mapping the UCR patterns of tobacco-rice and oilseed-rice, respectively. One metric, the

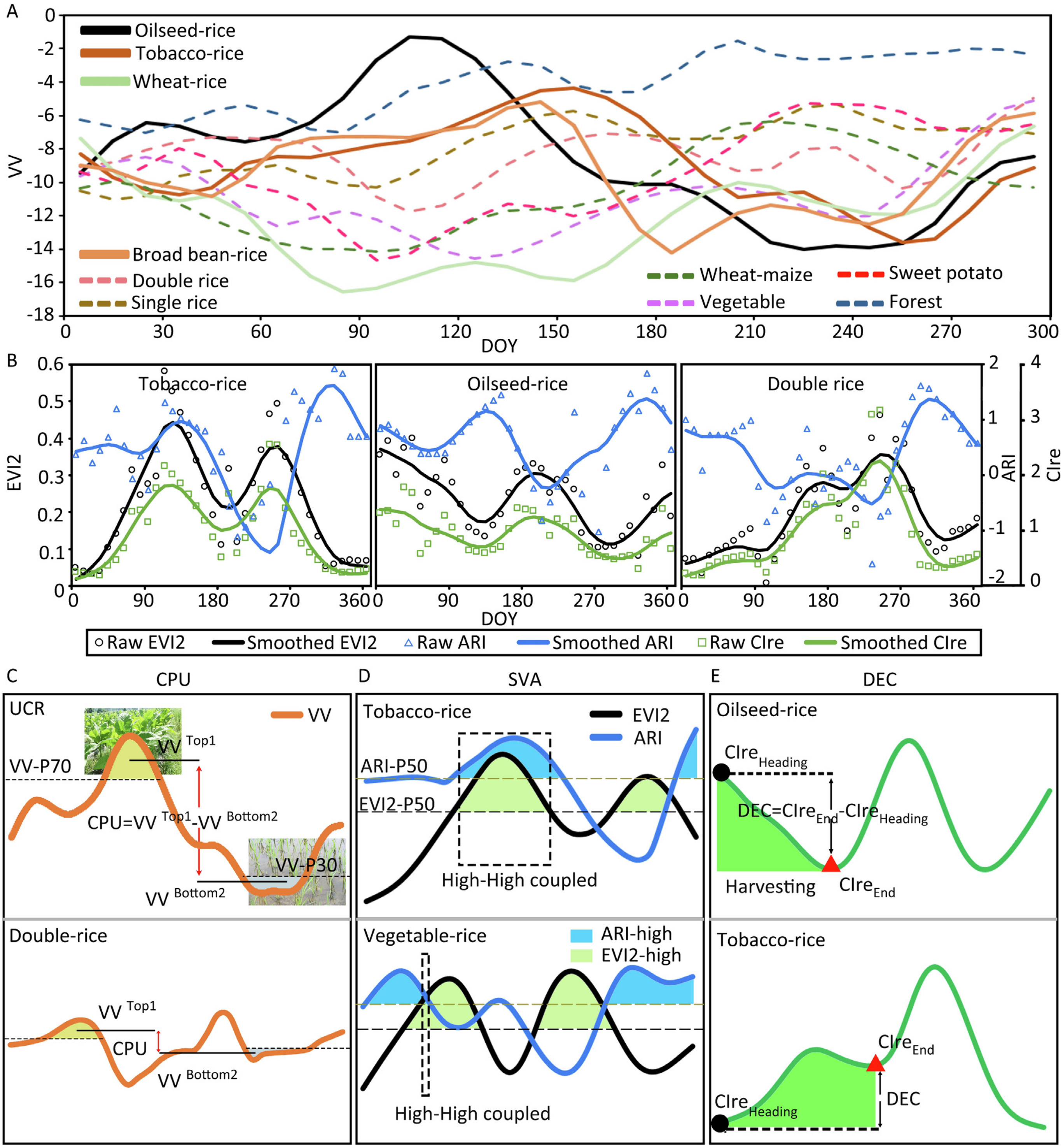

Fig. 3. Temporal profiles of different cropping patterns and knowledge-based CP indicators. (A) Sentinel-1 VV backscatters; (B) vegetation, CIre and ARI indices; and CP indicators of (C) CPU, (D) SVA, (E) DEC. Notes: VV-P30, VV-P70, EVI2-P50, ARI-P50 represent respectively the 30th and 70th VV temporal profiles and the 50th of EVI2 and ARI temporal profiles.

Synchronization of VI-ARI (SVA), was designed to measure the extent of co-existed positive waves of the VI-ARI temporal profiles (Fig. 3). The index of SVA was developed based on the frequency of co-occurred high values (high-high coupled pattern) from the VI-ARI time series within one year. Another index, the Decline of CIre (DEC) during the growing period, was developed to reveal the degree of decrease in Chl during the growing season (Fig. 3).

These two indicators are defined as:

$$SVA = \mathrm{Count}\left(VI^{High} \cap ARI^{High}\right)/N \tag{4}$$

$$DEC = Chl_{End}\text{-}Chl_{Heading} \tag{5}$$

Here VI^{High} and ARI^{High} represent the corresponding subsets of VI or ARI above the medium values during the study period; N is the number of observations in one year, which is 17 in this study (the temporal resolution was 10 d). The medium was exploited as the criteria for developing the CP index for identifying tobacco-UCR, instead of measuring the extent of consistent upward or download trends in the VI and ARI temporal profiles. This is because consistent trends are not the same as co-occurring high values in two time series (Fig. 3). Estimating dynamic trends for each observation is also more computation-intensive and the dynamic trends of time series are very sensitive to minor changes. The $Chl_{Heading}$ and Chl_{End} represent CIre values during the budding and harvesting stages of oilseed. The budding stages of winter oilseed are generally observed from late December to late Jan., and the maturing stages fall within the period from May to July in the study area. Winter oilseed shows high CIre values during the budding stage and low CIre values during the maturing stage. For this reason, the peaks in Jan. and the troughs during the period May–June were applied to represent the $Chl_{Heading}$ and Chl_{End} of the study year for that pixel.

3.5. Algorithm for mapping UCR patterns

The proposed RRSS algorithm was implemented based on the following procedures. First, the cropping practice of UCR was derived using the intra-seasonal VV indicator. Second, the UCR of tobacco rice was further extracted based on the VI-ARI coupled indicator. Finally, another major type of UCR, oilseed rice, was mapped using the Chl-based indicator.

$$\textit{if}\ (\mathrm{CPU} > \theta_1),\ \mathrm{URR} = 1;\textit{else}\ \mathrm{URR} = 0 \tag{6}$$

$$\textit{if}\ (\mathrm{URR} = 1)\ \&\ (\mathrm{SVA} > \theta_2),\ \mathrm{TR} = 1;\textit{else}\ \mathrm{TR} = 0 \tag{7}$$

$$\textit{if}\ (\mathrm{URR} = 1)\ \&\ (\mathrm{TR} = 0)\ \&\ (\mathrm{DEC} < \theta_3),\ \mathrm{OilR} = 1;\textit{else}\ \mathrm{OilR} = 0 \tag{8}$$

Here θ_1, θ_2 and θ_3 are constants and CPU, SVA, and DEC represent the respective values of these three proposed indicators (CPU, SVA, and DEC) (Fig. 3).

The cropping pattern of UCR can be directly mapped based on its corresponding CP indicator (CPU). The UCR-cultivated fields consistently showed higher CPU values. These two major UCR patterns, tobacco-UCR, and oilseed-UCR can be further derived from these two indicators developed by coupling greenness and pigment indices, the SVA and DEC, respectively. The proposed RRSS algorithm is expected to be robust to the intra-class variability of VI and SAR signals from rice cropping patterns. Even though there were phenological shifts or varied crop growth of UCR across different regions (Fig. 1), these indicators could consistently identify their targeted classes. The high-high VI-ARI coupled relationship remained unchanged during the growing season, due to the growth characteristic of tobacco (high anthocyanin concentration around heading stages) (Fig. 3).

3.6. Accuracy assessment

Validations of cropping patterns in single and double-mixed cropping regions are much more difficult than in single-cropping regions. Instantaneous field sampling data and agricultural census data are generally not quantified for the validation of the UCR mapping algorithm. This is because the agricultural census data reported the total sown area of major crops instead of the cropping patterns. Accuracy assessments were conducted primarily based on the reference sites. The user's, producer's, and overall accuracies, the kappa index, and the F1 scores were exploited for accuracy assessment of the UCR mapping algorithm [58]. The performance of the RRSS algorithm was assessed through visual comparisons and validated using representative reference areas in the XGM region.

4. Results

4.1. The 10-m UCR map in XGM region of South China based on S1 and S2

There were distinctive high values among the Dongting and Poyang Lake plains examined i the map of the proposed UCR indicator (Fig. 4). The designed UCR indicator was efficient in distinguishing UCR from cropland. The UCR cropped fields showed greater values in the UCR indicator (Fig. 4). The other two indicators, SVA and DEC, further discriminated tobacco-UCR and oilseed-UCR from the UCR-cultivated fields. In particular, the tobacco-UCR fields showed lower values (in blue) in the VI-ARI coupled index (SVA), and the oilseed-UCR fields showed large values (in bright green) in the Chl-based index (DEC). The efficiency of these three proposed UCR indicators was also indicated by some snapshots in Fujian and Jiangxi provinces (Fig. 4). Google Earth images and photos from the field survey revealed that the study area was characterized by fragmented cropland dominated by diverse and complex cropping systems including single rice, oilseed-rice, tobacco-rice, double rice, and others (Fig. 1C, 4).

The proposed RRSS algorithm was implemented in the study area and the first 10-m UCR data product was generated in the XGM region using Sentinel-1 SAR and Sentinel-2 MSI time series (Fig. 5). The planting areas of UCR were 7348 km^2 in 2021, and around one-half (48%) of UCR's planted area was distributed in plains. There were 5073 km^2 and 1128 km^2 areas of UCR fields rotated with oilseed and tobacco, which accounted for 69.04% and 15.35% of UCR in the study area, respectively. The oilseed UCR is widely distributed across the study area, especially on the Dongting Lake plain. The tobacco UCR is scattered among the mountains and hills, especially in the south of Hunan province and the west of Fujian province (Fig. 5). Only 29% of tobacco-rice UCR was located in plains, much lower than that from oilseed-rice UCR (52% cultivated in plains).

On the whole, the cropping pattern of UCR contributed to only one-tenth (9.20%) of the officially reported total sown areas of paddy rice (79,897 km^2) in the XGM region in 2021. The ratio of UCR to rice was low in the study area because around two thirds of rice-sown areas were cultivated in early rice or late rice (double rice) according to the officially reported data. There were no reported data on UCR cultivations and UCR practice was commonly implemented by winter or spring crops followed by middle rice (planted in June, which is later than early rice but earlier than late rice). The officially reported data of middle rice together with single cropping of late rice was 26,760 km^2, around one third of which was attributed to UCR.

4.2. Mapping accuracy of the RRSS algorithm

A total of 5197 reference sites were used to evaluate the mapping products of UCR in the XGM region. The confusion matrix of the UCR map is provided in Table 1. The accuracy assessment based on the reference sites suggested the good performance of the RRSS algorithm. The overall accuracy of the UCR map was 91.92% and the kappa index was 0.82. Classification of UCR achieved an F1 score of 0.88. The RRSS algorithm was capable of further distinguishing different UCR patterns in smallholder cropping systems. These 1525 UCR reference sites were further applied to validate the ability of RRSS to discriminating two major UCR patterns and the confusion matrix is shown in Table S1. An overall accuracy of 91.08% was obtained, with a kappa index of 0.86.

The classification of oilseed-UCR achieved a user accuracy of 91.89% and a producer accuracy of 90.76% (Table S1). Among these 649 reference sites of oilseed-UCR, 34 sites were misclassified as

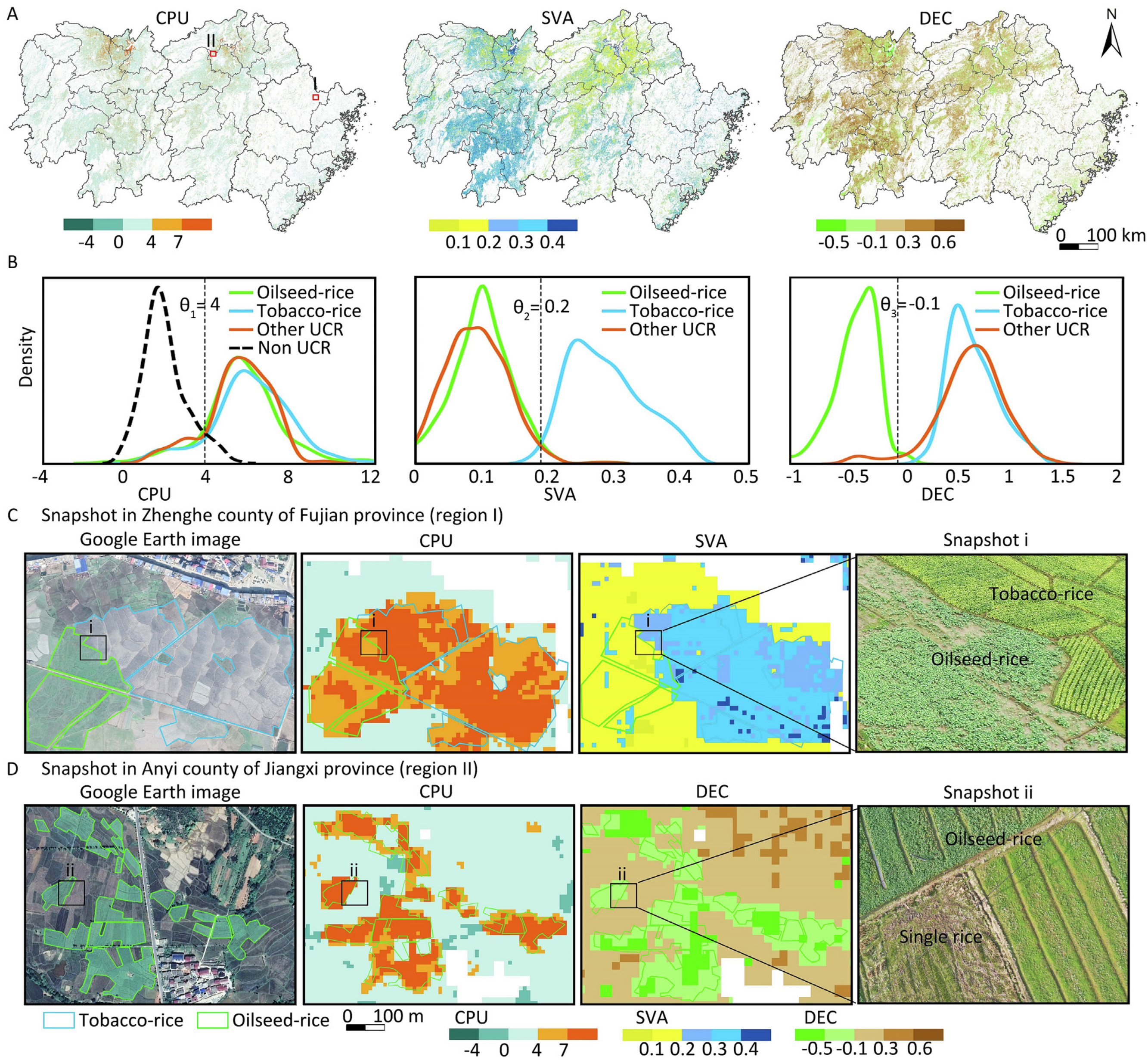

Fig. 4. Maps of (A) the three CP indicators, (B) the density, and some snapshots in (C) the Fujian and (D) Jiangxi provinces.

tobacco-UCR. For tobacco-UCR, 28 sites out of 491 sites were mislabeled as oilseed-UCR. Good accuracy was also obtained in mapping results of tobacco-UCR, although tobacco-UCR was scattered among mountainous and hilly regions. The F1 score of oilseed-UCR and tobacco-UCR was 0.91. Several oilseed-UCR or tobacco-UCR dominated areas or mixed planting areas were selected to show the mapping results more clearly (Fig. 5). The generated UCR maps are consistent with the visual-interpreted data using the drone imagery collected during the field survey. There were only some minor errors around the boundaries of the farmland plot, which were introduced by the salt and pepper phenomenon (roads or small houses). The RRSS algorithm can automatically distinguish different kinds of UCR types and generate finer-resolution maps at a large scale without local training or adjustments.

4.3. Spatiotemporal patterns of UCR in the XGM region during the period 2018–2021

The RRSS algorithm was transferred across different years and the UCR map in 2018 was obtained. The UCR maps in these two years (2018, 2021) illustrated fairly consistent spatial patterns (Fig. 5), which indicated that the UCR cultivation in the XGM region was stable in recent years. The UCR cultivated area was 7537.89 km^2 in 2018, which was slightly reduced by 2.52% (190.13 km^2) during the study period (2018–2021). The decline of UCR was due to the conversions of UCR to double rice (395.12 km^2) or upland crops (77.78 km^2), which were dominant in Jiangxi province and Fujian province, respectively (Fig. S3). The increase in UCR was mainly from single rice, which was dominant

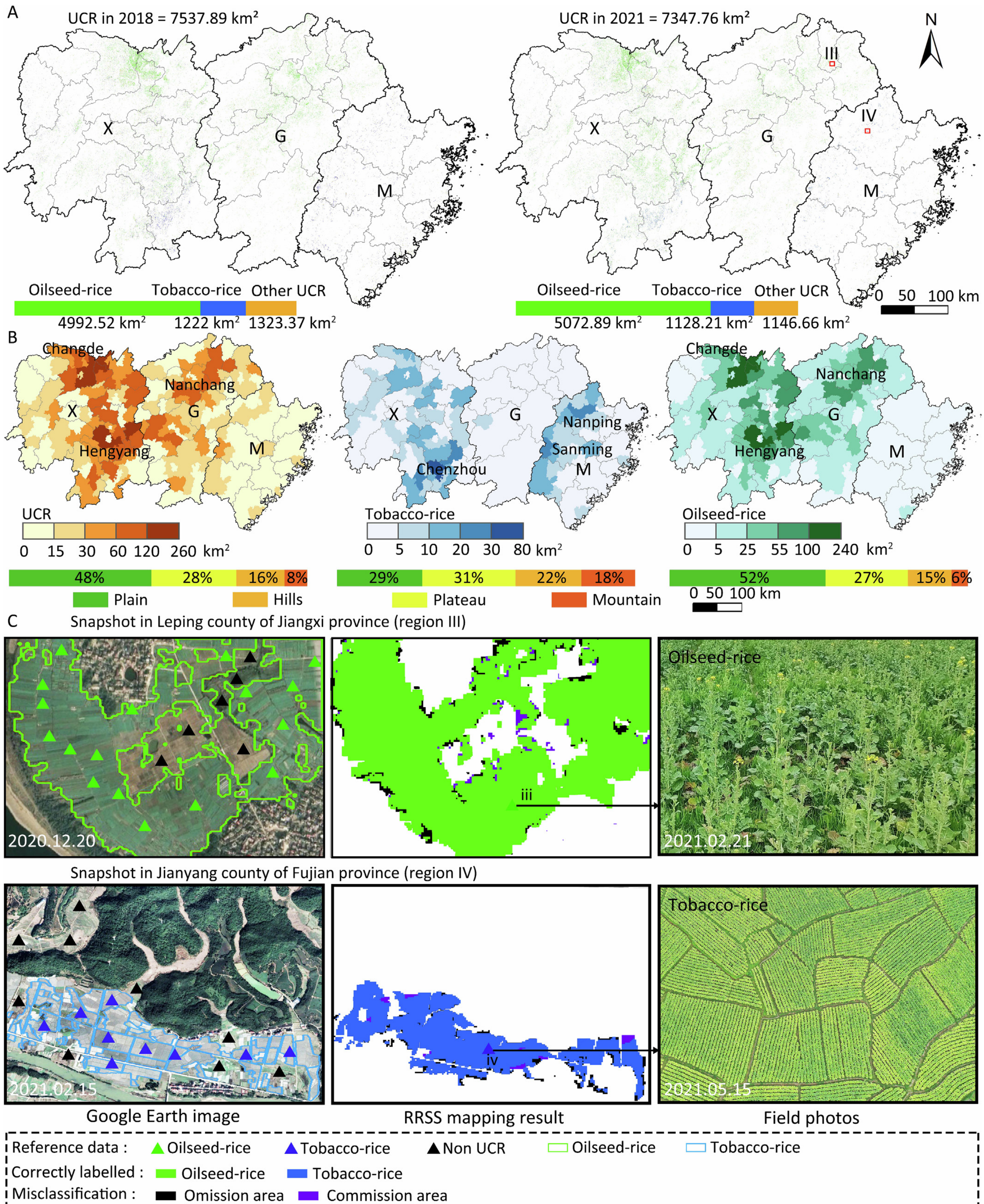

Fig. 5. Maps of (A) UCR in the XGM region in 2018 and 2021, (B) planted area of UCR, oilseed-rice, and tobacco-rice at the county level and their fractions in various topographies, and (C) some snapshots of RRSS mapping results in Jiangxi and Fujian provinces.

Table 1
Accuracy assessment on UCR map based on CP reference sites.

	Total	UCR	Non-UCR	Producer accuracy (%)	F1 score
UCR	1678	1525	153	90.88	0.88
Non-UCR	3519	267	3252	92.41	0.94
Total	5197	1792	3405		
User accuracy (%)		85.10	95.51		
Overall accuracy (%)	91.92				
Kappa	0.8184				

in the eastern and northern portions of Hunan province (Fig. 6). The net changes of UCR cultivated areas diversified among different provinces and UCR types. The slight reduction of UCR was jointly explained by the reductions of UCR in Jiangxi (377.48 km^2) and Fujian (107.19 km^2) provinces versus a large increase of UCR in Hunan province (294.52 km^2). The reduction of UCR was accounted for by the tobacco UCR and other UCR. The cultivated area of tobacco-UCR decreased by 7.67% in the study area, which was reduced by 94 km^2 during the study period 2018–2022. Differing from the tobacco-UCR, the oilseed-UCR slightly increased (by 80 km^2), especially in Hunan province (Fig. 6). There was a large increase (442 km^2, by 5.31%) in oilseed-UCR in Hunan province, compensating for the decline in Jiangxi province (Fig. 6).

According to the agricultural census data, 18,624 km^2 areas were cultivated in oilseeds in 2021. Thus, around one fourth (27.24%) of the oilseed sown area was rotated with paddy rice (cultivated by oilseed-UCR) in the XGM region. The lower proportions of oilseed-UCR were possibly accounted for by overestimations of oilseeds from the agricultural census data. The ratio of UCR to oilseed cropping was above 50% when the oilseed map was applied [57], which was 63.86% in Jiangxi and 54.95% in Hunan province (there was no oilseed map in Fujian province). To our knowledge, there was no tobacco map in the study area until now. According to the officially reported data, there were 1494 km^2 of tobacco. The tobacco-UCR dominated tobacco cultivation. Approximately three quarters (75.53%) of tobacco cultivation was performed as UCR in the study area.

5. Discussion

5.1. The advantages and limitations of phenological metrics/crop indices in large-scale crop mapping

Robust algorithms using crop indices or phenological metrics could highlight the target crop with little reliance on training data [52]. The crop indices have been developed to identify a series of crops such as paddy rice, winter wheat, and canola [56]. For example, the unique flooding signal of paddy rice has been exploited to establish rice mapping algorithms by incorporating vegetation and water indices, or recently by the V-shaped feature of backscattering [59,60]. These crop indices enlarged the differences between target crops and non-target crops by exploring the unique crop features of key phenological stages [56,61,62]. For example, the unique phenological feature and the unique flowering signal are critical for mapping winter wheat and oilseed [56,63,64].

Accurately estimating the phenological stages and exploring the unique crop features during key phenological stages is the foundation for discriminating crops [60]. Phenological information has been successfully applied for automatically mapping different crops [65]. There are three groups of phenological metrics commonly applied for agricultural mapping [66]. The first group is related to the phenological dates [67,68] or the length of phenological stages [69]. The second group is banding/spectral indices values of phenological date/stages [70]. The third group is the statistics of bands/spectral indices values among phenological dates/stages, such as the rate of changes and, zonal statistics [66,71] (Table S2). These phenological metrics have been successfully applied to crop mapping, primarily using the optical time series datasets [45]. Spectral properties at certain phenological phases are relatively consistent across regions and years [45].

Large-scale multiple crop type mapping is still challenging, particularly in smallholder complex farming systems [20,72]. There are at least two major groups of constraints for crop mapping in large-scale subtropical regions using phenological metrics/crop indices. One is the deficiency of methodology for deriving reliable datasets of phenological dates/stages, which play a key role in discriminating different crops. Another is the low data availability in the specific crop phenological dates/stages, which are commonly examined in subtropical regions with frequent cloud contaminations [57]. The phenological dates/stages could either be estimated by threshold-based algorithms or change detection methods [73]. However, the reliability depends on the assumption that the phenological stages correspond to a certain threshold or rapid changes in VI values, and there is no biophysical meaning for the selected threshold [73]. Phenological metrics detection accuracy varied among different methods, especially in tropical or subtropical regions with more frequent cloud contaminations [74].

Agricultural systems are expected to ensure sustainable food production to achieve the SDGs [20]. Asian countries produce over 90% of global rice and export to Africa and Europe [60]. China hosts the largest rice bowl and the highest rice production and consumption in the world [75]. There is distinctive spatiotemporal heterogeneity of rice cropping patterns (i.e., single rice, double rice, UCR) across regions [13]. Multiple cropping systems such as the UCR can promote food production and environmental sustainability [23]. Concerns about the sustainability of rice cropping systems demand accurate and updated maps of UCR with finer resolution at large scale [76]. The UCR is less investigated compared to other cropping patterns such as the winter wheat maize and double rice [17]. A robust mapping algorithm that can cope with these above challenges is urgently needed for generating accurate cropping pattern data products over complex large regions.

5.2. Automatic mapping in complex cropping systems: Moving from phenological metrics to robust CP indices

Recent agricultural remote sensing studies have moved from crop-type mapping to directly identifying crop sequences [28]. The practice of upload crop-rice cropping systems has been widely implemented for the benefit of increasing crop yields and improving soil health [23]. Cropping patterns mapping provides useful information for guiding sustainable agricultural management [27]. Accurately mapping crop patterns could enable targeting measures for mitigating challenges under the pressure of climate change [28,77]. Despite growing research interests in agricultural remote sensing, there is a deficiency of automatic and robust methodology for the direct identification of complex multiple cropping patterns such as UCR over large spatial domains [1]. This study filled this gap and the proposed RRSS algorithm demonstrated good performances in subtropical regions. Agricultural

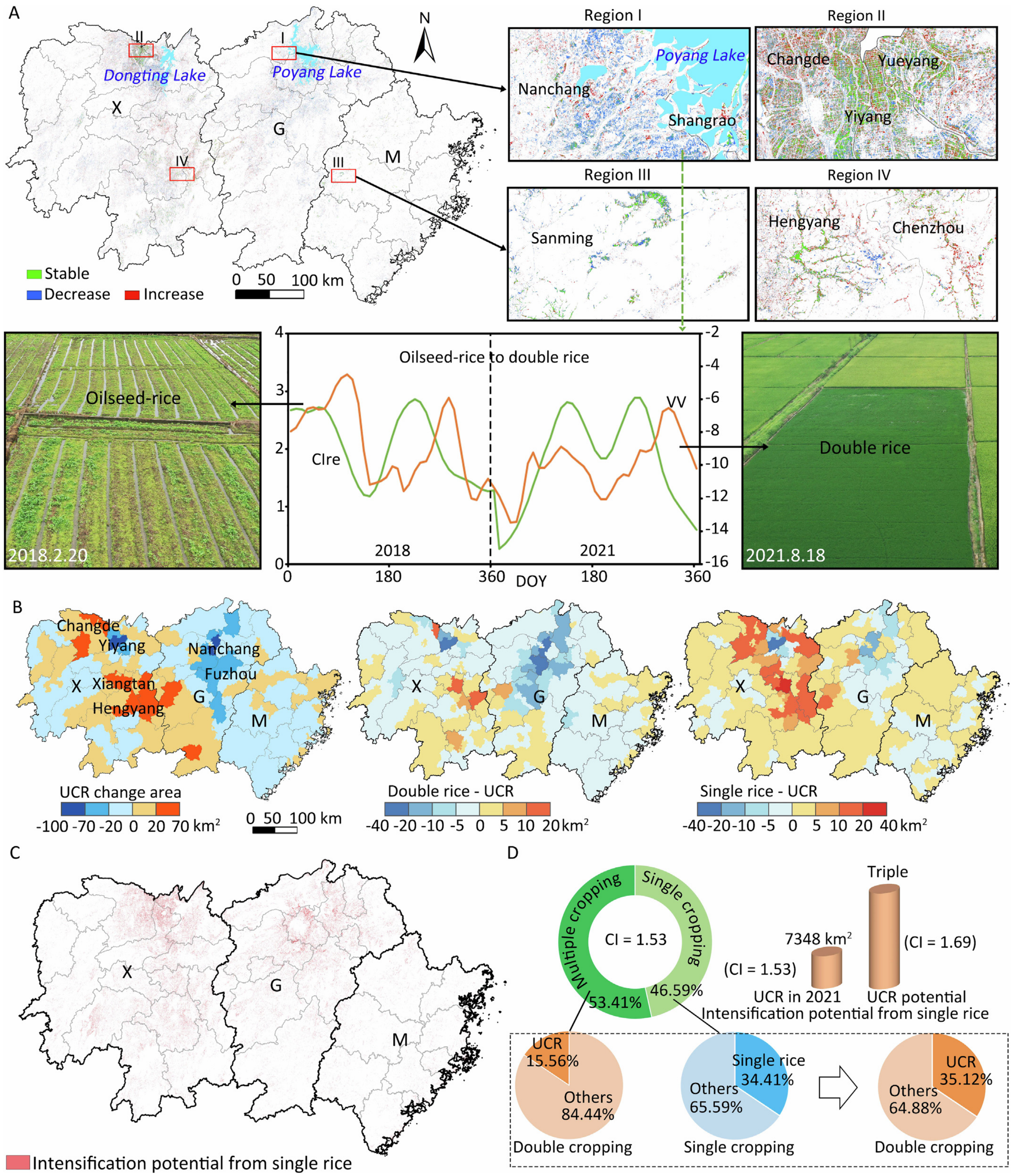

Fig. 6. CP changes in XGM region during 2018–2021. (A) map of UCR changes and some snapshots, (B) net change in UCR area at the county level; (C, D) map of intensification potential from single rice and (E) its contributions to intensifications.

mapping in tropical/subtropical regions is more complex due to the single- or double-mixed cropping systems, the flexible crop calendars, limited reference datasets irregular optical time series, and fragmented croplands [78]. The variable cropping frequency and crop phenology limit extensive applications of existing crop mapping approaches in regions without calibrations [60,79]. Datasets of cropping systems with information on crop sequences were generally derived based on annual crop type maps in the context of cropping intensity [80]. There are large uncertainties in existing data products of cropping intensity and crop types in South China dominated by small-holder farms and complex cropping systems [78,81].

This study moved from phenological metrics to robust CP metrics, which adaptively characterize the key features of UCR by coupling the temporal patterns of VI and pigment indices. Less frequently used red-edge or SWIR bands-based vegetation indices (VIs) may improve cropping pattern mapping [6]. Model performances can be improved by incorporating phenological metrics such as the lower quartile and median SAR values besides the phenophase information [66]. The design of the RRSS algorithm was inspired by previous knowledge-based crop mapping studies using phenological metrics or crop indices [66]. This study further developed the CP metric by engaging the zonal statistic of SAR signals, greenness, and anthocyanin index, which is more robust to intraclass variabilities when compared to approaches focusing on the local change characteristics [82]. The pigment concentration and variations during the crop-growing period reveal the internal physiological characteristics of crops [55]. The degree of temporal coupling between greenness and anthocyanin reflects the differences in temporal patterns in pigment concentration of growth season among different crops. Additionally, this study extended the within-season SAR-based metrics to inter-season features for characterizing the UCR cropping pattern [26,41]. For most crops, the VV backscatters generally followed an overall dynamic pattern of rise and drop during the growth period, which corresponded to the increase of biomass during the green stage and the decrease of canopy moisture during senescence [83]. Thus, the VV backscatters from the UCR-cropped fields achieved a strong increase during the green stage of the first crop, followed by a sharp decrease accounted by the bare soil after harvesting and further exacerbated by flooded fields during rice transplanting of the second crop.

The RRSS algorithm does not require these three key components under the classic crop mapping framework: information about cropping intensity (the number of valid cropping cycles or peaks), accurate phenology calendar, and abundant training datasets [41,84]. There are at least three major advantages of the RRSS algorithm. First, the RRSS algorithm is robust to the intraclass variabilities of optical and SAR signals from the same cropping patterns (Figs. 1, 3). These proposed CP indicators consistently highlight the targeted class by adaptively characterizing specific cropping patterns based on the dynamic patterns of SAR, vegetation, and pigment indices [6]. Second, the adaptive characterization of the annual time series datasets facilitates large-scale application with all available cloud-free observations, which is very significant for agricultural mapping among tropical or subtropical regions with infrequent satellite data [85,86]. Finally, the RRSS algorithm is fully operational for annual cropping pattern mapping with no requirements for localized adjustments, additional training datasets, or specific phenological stages [87]. The RRSS algorithm is simple and easy to understand, and can be employed to automatically discriminate UCR patterns from other cropping practices. These advantages of the RRSS algorithm promote its automatic application to single and double-mixed cropping systems, and can be used for generating national or even global annual UCR maps.

5.3. Mapping agricultural practices by fusing optical-SAR data for targeted sustainable intensification

Mapping cropping patterns at a regional scale requires the accessibility of dense time series images [6]. Sentinel-2 MSI data provides a unique opportunity for monitoring cropping patterns with finer spatiotemporal resolution. The unique red-edge bands of Sentinel-2 MSI images provide valuable information about leaf pigment and plant phenology [88]. Cropping pattern mapping can be improved by incorporating less frequently applied red-edge-based spectral indices and combined applications of optical and Synthetic Aperture Radar (SAR) data [6,29]. However, the problem with crop mapping using optical images is frequent cloud contamination, especially in rice-growing areas with rainy weather [59]. SAR images can continuously provide information on land surface roughness and canopy structures owing to the advantages of all-weather acquisition [88]. There is a great opportunity to generate finer-resolution large-scale agricultural systems maps with the support of GEE and the increasing availability of time series images [66,89]. Recent studies have successfully applied phenological metrics in agricultural land use monitoring based on S1 and S2 data [66]. These studies provide encouraging results and stimulate further research to estimate cropping practice including UCR at larger spatial domains through fusing optical-SAR data.

This study produced 10-m maps of two major UCR types in highly fragmented, single and double-mixed cropping systems, XGM regions, the most rice-productive regions in China. The generated UCR maps provided more detailed information on the crop sequences compared to previous efforts on specific crop type identification (i.e. oilseeds, paddy rice) [57,75]. Mapping minor crops such as tobacco is even more difficult compared to these staple crops because the spatial distribution is scattered [90]. These few studies on tobacco mapping were conducted on small areas using optical images [91,92]. To our knowledge, robust tobacco algorithms with the capability of extensive application have not been reported yet. This is the first time that multiple-cropped CP types, the oilseeds or tobacco-UCR, have been automatically mapped over large regions through a combined application of optical and SAR time series images.

There is increasing research interest in crop identification in recent decades and a series of datasets on crop types were generated in China [59]. Examples are the maps of single-season rice of 21 provincial administrative regions in China [93], maps of Rice Extent and Cropping Intensity (RECI data) in the XGM region (https://www.geodata.cn/data/datadetails.html?dataguid = 76460845139096&docId = 1) and the annual Oilseeds Extent Maps (REM) in the Yangtze River Economic Belt of China [57]. These crop datasets were generated by fusing S1 and S2 time series images, which achieved good accuracy [57]. These maps on specific crop types generally did not provide information on cropping intensity and crop sequences. A recent study [29] generated the cropping intensity dataset (CIChina10m) in China through improved quantifications of crop cycles based on the S1 and S2 time series. However, to our knowledge, there are no publicly available UCR datasets with descriptions of cropping sequences in the study area. Compared to oilseed, there is very limited research on tobacco mapping [91] and there are no spatial-explicit maps of tobacco cultivation in the XGM region.

The UCR accounted for 15.56% of multiple cropping according to the 10 m cropping intensity (CIChina10m) in China, based on the S1 and S2 time series data [29]. The XGM region is well adapted to multiple cropping owing to its abundant water and temperate conditions. However, roughly one half of cropped fields were cultivated in single cropping patterns such as single rice [29]. If the cultivation of single rice were intensified as CP of UCR, the UCR area could be tripled and the cropping intensity would be increased to 1.69 in 2021 in the XGM region (Fig. 6). If the cultivation of UCR intensified from single rice were implemented by multiple cropping system with oilseeds, the sown area of oilseeds would be doubled in comparison with Oilseeds Extent Maps (REM) data in Hunan and Jiangxi provinces [57]. The sown area of maximized oilseed-UCR from the intensification of single rice (13,469.84 km^2) corresponded roughly to the officially reported area (13,516 km^2).

This study provided the first UCR maps with descriptions of the crop sequences in southern China. Labor-intensive cash crops such as tobacco cultivation decreased in the past few years (Fig. 5). The decline of tobacco-UCR is expected to accelerate in the future, given that younger generations are reluctant to engage in labor-intensive tobacco farming. The oilseed-UCR experienced opposite trends in Hunan and Jiangxi provinces, two major rice-producing regions in China. The distinctively increased oilseed-UCR areas in Hunan province were stimulated by comparatively higher subsidies or even sowing by the local government with reference to our field survey data. In contrast, a reduction of oilseed-UCR was evidenced in Jiangxi province owing to the lower subsidies by the local government. There is still great potential for increasing UCR by intensification from single rice in southern China. Agricultural machinery and government subsidies are very important for ensuring the sustainable cropping patterns of UCR in southern China [7].

This study suggests that the RRSS algorithm is capable of extracting UCR fields and the crop sequences over subtropical regions where there is a flexible crop calendar of paddy rice and its cropping patterns. Most upland crops showed an inverted U-shaped temporal pattern from the Sentinel-1 VV time series, which enlarged the inter-seasonal backscatter ranges among UCR cropping systems. However, the cropping pattern of winter wheat-rice was not comprised in this study due to the opposite VV temporal patterns compared to other upland crops. The UCR fields rotated with tobacco were mapped based on the unique synchronous patterns of greenness and anthocyanin. However, UCR rotated with other solanaceous plants such as potato might show similar VI-ARI temporal patterns to the tobacco-UCR, resulting in commission errors. Future work could be conducted in the following areas: First, the proposed RRSS algorithm could be extended to identify more UCR types such as vegetable-rice and winter wheat-rice. Second, the RRSS algorithm should be further applied to other regions or countries based on fusing multimodal satellite time series datasets [26]. Finally, annual updated UCR dataset products could be generated in rice-producing countries such as China and India). Spatiotemporal changes among cropping patterns and their driving mechanisms could be investigated with combined considerations of biophysical and socio-economic variables (topographic conditions, cropland quality, agricultural labor, agricultural subsidy) to promote targeted sustainable intensification in developing countries.

6. Conclusions

This study developed a novel and robust algorithm for directly deriving multiple cropping systems of UCR in tropical regions with diverse topographic conditions and cropping systems. Existing crop mapping approaches were challenged by variable cropping frequency and crop phenology in single and double-mixed cropping regions. This study mitigated these challenges by designing robust metrics by exploring the distinctive inter-seasonal variations of VV backscatters introduced by upland-paddy rice cropping system. The proposed RRSS algorithm does not require accurately locating growth cycles or peaks, fixed temporal windows, and training datasets, which are the foundations of the classic crop mapping framework. This study opened a novel direction for developing crop indices based on the coupling of the temporal patterns of greenness and pigment concentrations. The first 10-m UCR maps of subtropical regions in South China were generated during the period 2018–2021, with an overall accuracy of 91.92% based on reference sites. There were 7348 km^2 areas implemented by UCR in 2021, which were mainly cultivated by oilseed-rice (69.04% of UCR area) and tobacco-rice (15.35% of UCR area). There are still great gaps in cropping intensity, which can boost UCR areas by three folds if filled by the cultivation of UCR in the XGM region. Finer-resolution maps of UCR types are required for promoting targeted sustainable intensification, given that rice feeds one half of the global population and can be intensified by multiple cropping with economic crops towards rural revitalization. The proposed RRSS algorithm demonstrated good performances in complex smallholder cropping systems, which can be further applied to generate national or global 10-m high-quality UCR products.

CRediT authorship contribution statement

Bingwen Qiu: Conceptualization, Methodology, Writing – original draft, Writing – review & editing, Project administration. **Linhai Yu:** Methodology, Investigation, Formal analysis. **Peng Yang:** Formal analysis, Writing – review & editing. **Wenbin Wu:** Writing – review & editing. **Jianfeng Chen:** Validation, Visualization. **Xiaolin Zhu:** Formal analysis. **Mingjie Duan:** Validation, Visualization.

Declaration of competing interest

The authors declare that they have no known competing financial interests or personal relationships that could have appeared to influence the work reported in this paper.

Acknowledgments

This work was supported by the National Natural Science Foundation of China (42171325, 41771468), the National Key Research and - Development Program of China (2022YFD2001101), the Science Bureau of Fujian Province (2023Y0042), and the Finance Department and the Digital Economy Alliance of Fujian Province. Thanks to our research group members and collaborators for collecting the ground reference data. We are very grateful to the editors and anonymous reviewers for offering insightful suggestions that significantly improve the manuscript.

Appendix A. Supplementary data

Supplementary data for this article can be found online at https://doi.org/10.1016/j.cj.2023.12.010.

References

[1] E.V. Upcott, P.A. Henrys, J.W. Redhead, S.G. Jarvis, R.F. Pywell, A new approach to characterising and predicting crop rotations using national-scale annual crop maps, Sci. Total Environ. 860 (2023) 160471.
[2] B. Rudiyanto, R.M. Minasny, N.C. Shah, C. Soh, B. Arif, Indra Setiawan, Automated near-real-time mapping and monitoring of rice extent, cropping patterns, and growth stages in Southeast Asia using Sentinel-1 time series on a Google Earth Engine platform, Remote Sens. 11 (2019) 1666.
[3] G. Zhang, X. Xiao, J. Dong, F. Xin, Y. Zhang, Y. Qin, R.B. Doughty, B. Moore, Fingerprint of rice paddies in spatial–temporal dynamics of atmospheric methane concentration in monsoon Asia, Nat. Commun. 11 (2020) 554.
[4] R. Dominschek, A.A.M. Barroso, C.R. Lang, A. de Moraes, R.M. Sulc, M.Z. Schuster, Crop rotations with temporary grassland shifts weed patterns and allows herbicide-free management without crop yield loss, J. Cleaner Prod. 306 (2021) 127140.
[5] A. Bégué, D. Arvor, B. Bellon, J. Betbeder, D. De Abelleyra, R.P.D. Ferraz, V. Lebourgeois, C. Lelong, M. Simões, S.R. Verón, Remote sensing and cropping practices: a review, Remote Sens. 10 (2018) 99.
[6] M. Mahlayeye, R. Darvishzadeh, A. Nelson, Cropping patterns of annual crops: a remote sensing review, Remote Sens. 14 (2022) 2404.
[7] M. Xiang, Q. Yu, Y. Li, Z. Shi, W. Wu, Increasing multiple cropping for land use intensification: the role of crop choice, Land Use Policy 112 (2022) 105846.
[8] J.D. Sachs, G. Schmidt-Traub, M. Mazzucato, D. Messner, N. Nakicenovic, J. Rockström, Six transformations to achieve the sustainable development goals, Nat. Sustain. 2 (2019) 805–814.
[9] Q. Li, X. Cao, K. Jia, M. Zhang, Q. Dong, Crop type identification by integration of high-spatial resolution multispectral data with features extracted from coarse-resolution time-series vegetation index data, Int. J. Remote Sens. 2014 (2014) 1–13.

[10] J. Han, Z. Zhang, J. Cao, Y. Luo, Mapping rapeseed planting areas using an automatic phenology- and pixel-based algorithm (APPA) in Google Earth Engine, Crop J. 10 (2022) 1483–1495.
[11] L. Wang, J. Wang, Z. Liu, J. Zhu, F. Qin, Evaluation of a deep-learning model for multispectral remote sensing of land use and crop classification, Crop J. 10 (2022) 1435–1451.
[12] H. Zheng, H. Huang, C. Zhang, J. Li, National-scale paddy-upland rotation in Northern China promotes sustainable development of cultivated land, Agric. Water Manage. 170 (2016) 20–25.
[13] K. Clauss, H. Yan, C. Kuenzer, Mapping paddy rice in China in 2002, 2005, 2010 and 2014 with MODIS time series, Remote Sens. 8 (2016) 434.
[14] Q. Hu, W. Hua, Y. Yin, X. Zhang, L. Liu, J. Shi, Y. Zhao, L. Qin, C. Chen, H. Wang, Rapeseed research and production in China, Crop J. 5 (2017) 127–135.
[15] Y. Fang, T. Ren, S. Zhang, Y. Liu, S. Liao, X. Li, R. Cong, J. Lu, Rotation with oilseed rape as the winter crop enhances rice yield and improves soil indigenous nutrient supply, Soil Tillage Res. 212 (2021) 105065.
[16] B. Qiu, X. Hu, C. Chen, Z. Tang, P. Yang, X. Zhu, C. Yan, Z. Jian, Maps of cropping patterns in China during 2015–2021, Sci. Data 9 (2022) 479.
[17] Z. Liu, Y. Liu, J. Dong, M.H.A. Baig, W. Chi, L. Peng, J. Wang, Patterns and causes of winter wheat and summer maize rotation area change over the North China Plain, Environ. Res. Lett. 17 (2022) 044056.
[18] G. Waldhoff, U. Lussem, G. Bareth, Multi-Data Approach for remote sensing-based regional crop rotation mapping: A case study for the Rur catchment, Germany, Int. J. Appl. Earth. Obs. 61 (2017) 55–69.
[19] M. Weiss, F. Jacob, G. Duveiller, Remote sensing for agricultural applications: a meta-review, Remote Sens. Environ. 236 (2020) 111402.
[20] L. Liu, X. Xiao, Y. Qin, J. Wang, X. Xu, Y. Hu, Z. Qiao, Mapping cropping intensity in China using time series Landsat and Sentinel-2 images and Google Earth Engine, Remote Sens. Environ. 239 (2020) 111624.
[21] B. Qiu, D. Lu, Z. Tang, D. Song, Y. Zeng, Z. Wang, C. Chen, N. Chen, H. Huang, W. Xu, Mapping cropping intensity trends in China during 1982–2013, Appl. Geogr. 79 (2017) 212–222.
[22] J. Han, Z. Zhang, Y. Luo, J. Cao, L. Zhang, H. Zhuang, F. Cheng, J. Zhang, F. Tao, Annual paddy rice planting area and cropping intensity datasets and their dynamics in the Asian monsoon region from 2000 to 2020, Agric. Syst. 200 (2022) 103437.
[23] Y. Liu, Q. Yu, Q. Zhou, C. Wang, S.D. Bellingrath-Kimura, W. Wu, Mapping the complex crop rotation systems in southern china considering cropping intensity, crop diversity, and their seasonal dynamics, IEEE J. Sel. Top. Appl. Earth Obs. Remote Sens. 15 (2022) 9584–9598.
[24] S. Estel, T. Kuemmerle, C. Levers, M. Baumann, P. Hostert, Mapping cropland-use intensity across Europe using MODIS NDVI time series, Environ. Res. Lett. 11 (2016) 024015.
[25] L. Carrasco, G. Fujita, K. Kito, T. Miyashita, Historical mapping of rice fields in Japan using phenology and temporally aggregated Landsat images in Google Earth Engine, ISPRS-J. Photogramm. Remote Sens. 91 (2022) 277–289.
[26] L. Blickensdörfer, M. Schwieder, D. Pflugmacher, C. Nendel, S. Erasmi, P. Hostert, Mapping of crop types and crop sequences with combined time series of Sentinel-1, Sentinel-2 and Landsat 8 data for Germany, Remote Sens. Environ. 269 (2022) 112831.
[27] R. Li, M. Xu, Z. Chen, B. Gao, J. Cai, F. Shen, X. He, Y. Zhuang, D. Chen, Phenology-based classification of crop species and rotation types using fused MODIS and Landsat data: The comparison of a random-forest-based model and a decision-rule-based model, Soil Tillage Res. 206 (2021) 104838.
[28] G.L. Feyisa, L.K. Palao, A. Nelson, M.K. Gumma, A. Paliwal, K.T. Win, K.H. Nge, D. E. Johnson, Characterizing and mapping cropping patterns in a complex agro-ecosystem: An iterative participatory mapping procedure using machine learning algorithms and MODIS vegetation indices, Comput. Electron. Agric. 175 (2020) 105595.
[29] B. Qiu, X. Hu, P. Yang, Z. Tang, W. Wu, Z. Li, A robust approach for large-scale cropping intensity mapping in smallholder farms from vegetation, brownness indices and SAR time series, ISPRS-J. Photogramm. Remote Sens. 203 (2023) 328–344.
[30] B. Pan, Y. Zheng, R. Shen, T. Ye, W. Zhao, J. Dong, H. Ma, W. Yuan, High resolution distribution dataset of double-season paddy rice in china, Remote Sens. 13 (2021) 4609.
[31] A. Veloso, S. Mermoz, A. Bouvet, T. le Toan, M. Planells, J.-F. Dejoux, E. Ceschia, Understanding the temporal behavior of crops using Sentinel-1 and Sentinel-2-like data for agricultural applications, Remote Sens. Environ. 199 (2017) 415–426.
[32] P.H.C. Eilers, A perfect smoother, Anal. Chem. 75 (2003) 3631–3636.
[33] M.-J. Lambert, P.C.S. Traoré, X. Blaes, P. Baret, P. Defourny, Estimating smallholder crops production at village level from Sentinel-2 time series in Mali's cotton belt, Remote Sens. Environ. 216 (2018) 647–657.
[34] Z. Jiang, A.R. Huete, K. Didan, T. Miura, Development of a two-band enhanced vegetation index without a blue band, Remote Sens. Environ. 112 (2008) 3833–3845.
[35] A.A. Gitelson, M.N. Merzlyak, O.B. Chivkunova, Optical properties and nondestructive estimation of anthocyanin content in plant leaves, Photochem. Photobiol. 74 (2001) 38–45.
[36] J. Chen, J. Chen, A. Liao, X. Cao, L. Chen, X. Chen, C. He, G. Han, S. Peng, M. Lu, Global land cover mapping at 30 m resolution: a POK-based operational approach, ISPRS-J. Photogramm. Remote Sens. 103 (2015) 7–27.
[37] L. Zhong, L. Hu, H. Zhou, X. Tao, Deep learning based winter wheat mapping using statistical data as ground references in Kansas and northern Texas, US, Remote Sens. Environ. 233 (2019) 111411.
[38] Y. Song, J. Wang, Mapping winter wheat planting area and monitoring its phenology using Sentinel-1 backscatter time series, Remote Sens. 11 (2019) 449.
[39] Y. Wen, X. Li, H. Mu, L. Zhong, H. Chen, Y. Zeng, S. Miao, W. Su, P. Gong, B. Li, J. Huang, Mapping corn dynamics using limited but representative samples with adaptive strategies, ISPRS-J. Photogramm. Remote Sens. 190 (2022) 252–266.
[40] H.R. Kerner, R. Sahajpal, D.B. Pai, S. Skakun, E. Puricelli, M. Hosseini, S. Meyer, I. Becker-Reshef, Phenological normalization can improve in-season classification of maize and soybean: a case study in the central US Corn Belt, Sci. Remote Sens. 6 (2022) 100059.
[41] R. d'Andrimont, A. Verhegghen, G. Lemoine, P. Kempeneers, M. Meroni, M. van der Velde, From parcel to continental scale – A first European crop type map based on Sentinel-1 and LUCAS Copernicus in-situ observations, Remote Sens. Environ 266 (2021) 112708.
[42] B. Qiu, Y. Luo, Z. Tang, C. Chen, D. Lu, H. Huang, Y. Chen, N. Chen, W. Xu, Winter wheat mapping combining variations before and after estimated heading dates, ISPRS-J. Photogramm. Remote Sens. 123 (2017) 35–46.
[43] Z. Wang, H. Zhang, W. He, L. Zhang, Cross-phenological-region crop mapping framework using Sentinel-2 time series Imagery: A new perspective for winter crops in China, ISPRS-J. Photogramm. Remote Sens. 193 (2022) 200–215.
[44] J. Dong, Y. Fu, J. Wang, H. Tian, S. Fu, Z. Niu, W. Han, Y. Zheng, J. Huang, W. Yuan, Early-season mapping of winter wheat in China based on Landsat and Sentinel images, Earth Syst. Sci. Data 12 (2020) 3081–3095.
[45] L. Zhong, L. Hu, L. Yu, P. Gong, G.S. Biging, Automated mapping of soybean and corn using phenology, ISPRS-J. Photogramm. Remote Sens. 119 (2016) 151–164.
[46] J. Gray, M. Friedl, S. Frolking, N. Ramankutty, A. Nelson, M. Gumma, Mapping Asian cropping intensity with MODIS, IEEE J. Sel. Top. Appl. Earth Obs. Remote Sens. 7 (2014) 3373–3379.
[47] M.K. Gumma, P.S. Thenkabail, P. Panjala, P. Teluguntla, T. Yamano, I. Mohammed, Multiple agricultural cropland products of South Asia developed using Landsat-8 30 m and MODIS 250 m data using machine learning on the Google Earth Engine (GEE) cloud and spectral matching techniques (SMTs) in support of food and water security, GISci. Remote Sens. 59 (2022) 1048–1077.
[48] M. Zhang, B. Wu, H. Zeng, G. He, C. Liu, S. Tao, Q. Zhang, M. Nabil, F. Tian, J. Bofana, GCI30: a global dataset of 30-m cropping intensity using multisource remote sensing imagery, Earth Syst. Sci. Data Discuss. 13 (2021) 4799–4817.
[49] K. Clauss, M. Ottinger, C. Kuenzer, Mapping rice areas with Sentinel-1 time series and superpixel segmentation, Int. J. Remote Sens. 39 (2018) 1399–1420.
[50] X. Huang, M. Reba, A. Coffin, B.R.K. Runkle, Y. Huang, B. Chapman, B. Ziniti, S. Skakun, S. Kraatz, P. Siqueira, N. Torbick, Cropland mapping with L-band UAVSAR and development of NISAR products, Remote Sens. Environ. 253 (2021) 112180.
[51] Y. Guo, X. Jia, D. Paull, J.A. Benediktsson, Nomination-favoured opinion pool for optical-SAR-synergistic rice mapping in face of weakened flooding signals, ISPRS-J. Photogramm. Remote Sens. 155 (2019) 187–205.
[52] S. Xu, X. Zhu, J. Chen, X. Zhu, M. Duan, B. Qiu, L. Wan, X. Tan, Y.N. Xu, R. Cao, A robust index to extract paddy fields in cloudy regions from SAR time series, Remote Sens. Environ. 285 (2023) 113374.
[53] H. Bazzi, N. Baghdadi, M. El Hajj, M. Zribi, D.H.T. Minh, E. Ndikumana, D. Courault, H. Belhouchette, Mapping paddy rice using Sentinel-1 SAR time series in Camargue, France, Remote Sens. 11 (2019) 887.
[54] S. Hörtensteiner, B. Kräutler, Chlorophyll breakdown in higher plants, Biochim. Biophys. Acta - Bioenerg. 2011 (1807) 977–988.
[55] M.N. Merzlyak, O.B. Chivkunova, A.E. Solovchenko, K.R. Naqvi, Light absorption by anthocyanins in juvenile, stressed, and senescing leaves, J. Exp. Bot. 59 (2008) 3903–3911.
[56] D. Ashourloo, H.S. Shahrabi, M. Azadbakht, H. Aghighi, H. Nematollahi, A. Alimohammadi, A.A. Matkan, Automatic canola mapping using time series of sentinel 2 images, ISPRS-J. Photogramm. Remote Sens. 156 (2019) 63–76.
[57] W. Liu, H. Zhang, Mapping annual 10 m rapeseed extent using multisource data in the Yangtze River Economic Belt of China (2017–2021) on Google Earth Engine, Int. J. Appl. Earth. Obs. 117 (2023) 103198.
[58] G. Hripcsak, A.S. Rothschild, Agreement, the f-measure, and reliability in information retrieval, J. Am. Med Inform. Assn. 12 (2005) 296–298.
[59] P. Zhan, W. Zhu, N. Li, An automated rice mapping method based on flooding signals in synthetic aperture radar time series, Remote Sens. Environ. 252 (2021) 112112.
[60] J. Dong, X. Xiao, Evolution of regional to global paddy rice mapping methods: a review, ISPRS-J. Photogramm. Remote Sens. 119 (2016) 214–227.
[61] Y. Pan, L. Li, J. Zhang, S. Liang, X. Zhu, D. Sulla-Menashe, Winter wheat area estimation from MODIS-EVI time series data using the Crop Proportion Phenology Index, Remote Sens. Environ. 119 (2012) 232–242.
[62] H. Tian, T. Chen, Q. Li, Q. Mei, S. Wang, M. Yang, Y. Wang, Y. Qin, A novel spectral index for automatic canola mapping by using sentinel-2 imagery, Remote Sens. 14 (2022) 1113.
[63] Y. Zang, X. Chen, J. Chen, Y. Tian, Y. Shi, X. Cao, X. Cui, Remote sensing index for mapping canola flowers using MODIS data, Remote Sens. 12 (2020) 3912.
[64] C. Qu, P. Li, C. Zhang, A spectral index for winter wheat mapping using multi-temporal Landsat NDVI data of key growth stages, ISPRS-J. Photogramm. Remote Sens. 175 (2021) 431–447.
[65] D. Ashourloo, H. Nematollahi, A. Huete, H. Aghighi, M. Azadbakht, H.S. Shahrabi, S. Goodarzdashti, A new phenology-based method for mapping wheat and barley using time-series of Sentinel-2 images, Remote Sens. Environ. 280 (2022) 113206.

[66] A.-K. Holtgrave, N. Röder, A. Ackermann, S. Erasmi, B. Kleinschmit, Comparing Sentinel-1 and -2 data and indices for agricultural land use monitoring, Remote Sens. 12 (2020) 2919.
[67] A. Htitiou, A. Boudhar, A. Chehbouni, T. Benabdelouahab, National-scale cropland mapping based on phenological metrics, environmental covariates, and machine learning on Google Earth Engine, Remote Sens. 13 (2021) 4378.
[68] R. Sianturi, V.G. Jetten, J. Sartohadi, Mapping cropping patterns in irrigated rice fields in West Java: towards mapping vulnerability to flooding using time-series MODIS imageries, Int. J. Appl. Earth. Obs. 66 (2018) 1–13.
[69] G.R. Aduvukha, E.M. Abdel-Rahman, A.W. Sichangi, G.O. Makokha, T. Landmann, B.T. Mudereri, H.E.Z. Tonnang, T. Dubois, Cropping pattern mapping in an agro-natural heterogeneous landscape using sentinel-2 and sentinel-1 satellite datasets, Agriculture 11 (2021) 530.
[70] D. Ashourloo, H.S. Shahrabi, M. Azadbakht, A.M. Rad, H. Aghighi, S. Radiom, A novel method for automatic potato mapping using time series of Sentinel-2 images, Comput. Electron. Agric. 175 (2020) 105583.
[71] F. Xuan, Y. Dong, J. Li, X. Li, W. Su, X. Huang, J. Huang, Z. Xie, Z. Li, H. Liu, W. Tao, Y. Wen, Y. Zhang, Mapping crop type in Northeast China during 2013–2021 using automatic sampling and tile-based image classification, Int. J. Appl. Earth. Obs. 117 (2023) 103178.
[72] L. You, Z. Sun, Mapping global cropping system: Challenges, opportunities, and future perspectives, Crop Environ. 1 (2022) 68–73.
[73] L. Zeng, B.D. Wardlow, D. Xiang, S. Hu, D. Li, A review of vegetation phenological metrics extraction using time-series, multispectral satellite data, Remote Sens. Environ. 237 (2020) 111511.
[74] B. Qiu, M. Feng, Z. Tang, A simple smoother based on continuous wavelet transform: Comparative evaluation based on the fidelity, smoothness and efficiency in phenological estimation, Int. J. Appl. Earth. Obs. 47 (2016) 91–101.
[75] G. Zhang, X. Xiao, C.M. Biradar, J. Dong, Y. Qin, M.A. Menarguez, Y. Zhou, Y. Zhang, C. Jin, J. Wang, R.B. Doughty, M. Ding, B. Moore Iii, Spatiotemporal patterns of paddy rice croplands in China and India from 2000 to 2015, Sci. Total Environ. 579 (2017) 82–92.
[76] J. Wang, X. Xiao, Y. Qin, J. Dong, G. Zhang, W. Kou, C. Jin, Y. Zhou, Y. Zhang, Mapping paddy rice planting area in wheat-rice double-cropped areas through integration of Landsat-8 OLI, MODIS and PALSAR images, Sci. Rep. 5 (2015) 10088.
[77] H. Li, Y. Tian, C. Zhang, S. Zhang, P.M. Atkinson, Temporal Sequence Object-based CNN (TS-OCNN) for crop classification from fine resolution remote sensing image time-series, Crop J. 10 (2022) 1507–1516.
[78] Y. He, J. Dong, X. Liao, L. Sun, Z. Wang, N. You, Z. Li, P. Fu, Examining rice distribution and cropping intensity in a mixed single- and double-cropping region in South China using all available Sentinel 1/2 images, Int. J. Appl. Earth. Obs. 101 (2021) 102351.
[79] R. Fatchurrachman, N.C. Soh, R.M. Shah, S.G.E. Giap, B.I. Setiawan, B. Minasny, High-resolution mapping of paddy rice extent and growth stages across peninsular malaysia using a fusion of Sentinel-1 and 2 time series data in Google Earth Engine, Remote Sens. 14 (2022) 1875.
[80] P. Rufin, D. Frantz, S. Ernst, A. Rabe, P. Griffiths, M. Özdoğan, P. Hostert, Mapping cropping practices on a national scale using intra-annual Landsat time series binning, Remote Sens. 11 (2019) 232.
[81] B. Qiu, D. Lin, C. Chen, P. Yang, Z. Tang, Z. Jin, Z. Ye, X. Zhu, M. Duan, H. Huang, Z. Zhao, W. Xu, Z. Chen, From cropland to cropped field: A robust algorithm for national-scale mapping by fusing time series of Sentinel-1 and Sentinel-2, Int. J. Appl. Earth. Obs. 113 (2022) 103006.
[82] B. Qiu, F. Jiang, C. Chen, Z. Tang, W. Wu, J. Berry, Phenology-pigment based automated peanut mapping using sentinel-2 images, GISci. Remote Sens. 58 (2021) 1–17.
[83] A. Mercier, J. Betbeder, J. Baudry, V. Le Roux, F. Spicher, J. Lacoux, D. Roger, L. Hubert-Moy, Evaluation of Sentinel-1 & 2 time series for predicting wheat and rapeseed phenological stages, ISPRS-J. Photogramm. Remote Sens. 163 (2020) 231–256.
[84] H. Chen, H. Li, Z. Liu, C. Zhang, S. Zhang, P.M. Atkinson, A novel Greenness and Water Content Composite Index (GWCCI) for soybean mapping from single remotely sensed multispectral images, Remote Sens. Environ. 295 (2023) 113679.
[85] B. Qiu, D. Lu, Z. Tang, C. Chen, F. Zou, Automatic and adaptive paddy rice mapping using Landsat images: case study in Songnen Plain in Northeast China, Sci. Total Environ. 598 (2017) 581–592.
[86] H. Zhang, W. Liu, L. Zhang, Seamless and automated rapeseed mapping for large cloudy regions using time-series optical satellite imagery, ISPRS-J. Photogramm. Remote Sens. 184 (2022) 45–62.
[87] Y. Gao, Y. Pan, X. Zhu, L. Li, S. Ren, C. Zhao, X. Zheng, FARM: A fully automated rice mapping framework combining Sentinel-1 SAR and Sentinel-2 multi-temporal imagery, Comput. Electron. Agric. 213 (2023) 108262.
[88] A. Orynbaikyzy, U. Gessner, B. Mack, C. Conrad, Crop type classification using fusion of Sentinel-1 and Sentinel-2 data: assessing the impact of feature selection, optical data availability, and parcel sizes on the accuracies, Remote Sens. 12 (2020) 2779.
[89] H. Li, X.-P. Song, M.C. Hansen, I. Becker-Reshef, B. Adusei, J. Pickering, L. Wang, L. Wang, Z. Lin, V. Zalles, P. Potapov, S.V. Stehman, C. Justice, Development of a 10-m resolution maize and soybean map over China: Matching satellite-based crop classification with sample-based area estimation, Remote Sens. Environ. 294 (2023) 113623.
[90] G. Peng, L. Deng, W. Cui, T. Ming, W. Shen, Remote sensing monitoring of tobacco field based on phenological characteristics and time series image—a case study of Chengjiang County, Yunnan Province, China, Chin. Geogr. Sci. 19 (2009) 186–193.
[91] C. Maguranyanga, A. Murwira, Mapping maize, tobacco, and soybean fields in large-scale commercial farms of Zimbabwe based on multitemporal NDVI images in MAXENT, Can. J. Remote Sens. 40 (2014) 396–405.
[92] X. Zhu, G. Xiao, P. Wen, J. Zhang, C. Hou, Mapping tobacco fields using UAV RGB images, Sensors 19 (2019) 1791.
[93] R. Shen, B. Pan, Q. Peng, J. Dong, X. Chen, X. Zhang, T. Ye, J. Huang, W. Yuan, High-resolution distribution maps of single-season rice in China from 2017 to 2022, Earth Syst. Sci. Data 15 (2023) 3203–3222.